Hindawi
Journal of Control Science and Engineering
Volume 2021, Article ID 6621060, 11 pages
https://doi.org/10.1155/2021/6621060

Research Article

A Novel Real-Time Center of Gravity Estimation Method for Wheel Loaders with Front/Rear-Axle-Independent Electric Driving

Zhiyu Yang[1], **Jixin Wang**[2] **and Yunwu Han**[3]

[1]*Chongqing Key Laboratory of Manufacturing Equipment Mechanism Design and Control, Chongqing Technology and Business University, Chongqing 400067, China*
[2]*School of Mechanical and Aerospace Engineering, Jilin University, Changchun 130025, China*
[3]*School of Intelligent Transportation, Jiangsu Vocational College of Electronics and Information, Huaian 223003, China*

Correspondence should be addressed to Yunwu Han; 917946826@qq.com

Received 16 November 2020; Revised 25 April 2021; Accepted 15 May 2021; Published 31 May 2021

Academic Editor: Radek Matušů

Estimation of the center of gravity (CG) is the basis for intelligent control of the front-and-rear-axis-independent electric driving wheel loaders (FREWLs). This paper presents a novel real-time method for estimating the CG of FREWLs, which is suitable for driving and spading conditions on bumpy roads. A FREWL dynamical model is proposed to set up the state-space model. The CG estimator is used to estimate the longitudinal tire force using the state-space model and the improved square-root unscented Kalman filter (ISR-UKF) algorithm. The simulation and experimental results indicate that this method is suitable for FREWL dynamics and operational characteristics, and the estimated value of CG basically converges to the reference value. Finally, the probable reasons for error occurring in two experiments and the practical challenges of this method are discussed. The research in this paper establishes a partial theoretical basis for intelligent control of construction machinery.

1. Introduction

Intelligent control is the main development trend for wheel loaders [1–3]. A method of estimating the center of gravity (CG) is a core technique for intelligent control of the longitudinal motion of machinery. When the wheel loader is operating in complex operating conditions, the wheels often slip because of the large spading force. According to the wheel loader dynamic model and correlation vehicle theory, the determination of the CG location accurately is an effective approach to realize precise longitudinal control of loader and prevent wheels slipping. However, there is little research on CG estimation of wheel loaders at present, which restricts the development of this technology.

We performed a literature search on methods that have been used for vehicle state estimation, especially vehicle CG estimation. Ding et al. [4] proposed an enabling multisensor fusion-based longitudinal vehicle speed estimator by Kalman filters for four-wheeled independently actuated electric vehicles. Wang et al. [5] established a nonlinear suspension model and a rolling plane vehicle model used for estimating the roll angle and rate by an adaptive extended Kalman filter. In the meantime, the forgetting factor recursive least-squares (FFRLS) method is utilized to identify the CG of the vehicle. Wang et al. [6] designed a new type of particle filter (PF) and applied to Lyapunov stability theory estimating tire lateral forces.

The methods of CG estimation in the literature can be classified into the following three categories: Kalman filter methods, recursive least-squares methods, and extended Kalman filter (EKF) methods. Lee et al. [7] used the relationship between the ratio of rear-to-front tire longitudinal force and the corresponding wheel slips to determine the real-time vehicle CG location. Kim [8] estimated it using an inertial-parameter-measurement device at a vehicle-inertial-measurement facility. This method requires knowledge of vehicle weight, driving axle, and roof height prior to measurement. Huang and Wang [9] presented a real-time estimation method for vehicle CG using EKF in longitudinal maneuvers with road-course elevation. Huang and Wang

[10] also utilized the instant effective radius by employing a Kalman filter to perform online estimation of CG height for lightweight vehicles. To avoid lateral/yaw/roll excitations, Huang and Wang [11] estimated the real-time CG position for lightweight vehicles based on a combined adaptive Kalman filter-extended Kalman filter approach. Yue et al. [12] presented a braking-detection method using a dynamic braking model to estimate the vehicle's CG height. Chen et al. [13] used a parameter estimator that included Kalman filtering and the recursive least-squares method with a variable forgetting factor to estimate the CG position of a four-wheeled independently driven electronic vehicle. Yu and Wang [14] presented an estimation method based on Ackermann's steering geometry. This method is able to estimate multiple vehicles' CG positions and inertial parameters simultaneously. Lin et al. [15] utilized an approach to estimate the CG position of electric vehicles basing on a combined H∞ filter and EKF.

The above approaches have been successful in the vehicle field. Some of the algorithms have the ability to dynamically estimate the center of gravity position of the vehicle, and the estimation accuracy is high. However, due to the limitations of Kalman filter methods, recursive least-squares methods, and extended Kalman filter (EKF) methods, their ability to estimate strongly nonlinear problems is weak so that it is difficult to apply them to wheel loaders in complex operating conditions.

On the one hand, the structure, dynamical model, and operating characteristics differ greatly between wheel loaders and conventional vehicles, which mainly reflect in that wheel loaders have added extra working equipment, and spading force should be considered in the dynamic analysis. On the other hand, because the operational characteristics of wheel loaders have obvious volatility and periodicity in the spading condition on a bumpy road, the CG estimation model based on the dynamic model of the wheel loader is strongly nonlinear, and the Kalman filter and EKF are weak in dealing with strongly nonlinear problems, making it difficult to find real-time values under drastic changes in the operation stage.

This paper proposes a novel CG estimation method for front/rear-axle-independent electric driving wheel loaders (FREWLs). This method is suitable for wheeled construction machinery. In order to reinforce the method's ability to solve strongly nonlinear problems, the estimator applies an improved square-root unscented Kalman filter (ISR-UKF) algorithm. The ISR-UKF avoids the problem of having a negative-definite Cholesky factor [16], making it greater than the traditional unscented Kalman filter [17, 18] on computational stability.

The rest of the paper is organized as follows. The transmission structure and longitudinal dynamic model of the FREWLs are presented in Section 2. The real-time FREWL CG estimator is proposed in Section 3. Simulation studies and analysis considering driving and spading conditions on bumpy roads are proposed in Section 4. Section 5 presents the experimental validation results obtained from FREWL road tests. The probable reasons for error in two experiments and the challenges of this method in practice are discussed in Section 6.

2. FREWL Dynamic Model

The FREWL is a novel series of hybrid wheel loaders. The principles of the transmission structure and the structure of the experimental platform are shown in Figures 1 and 2, respectively. The front/rear-axle motor can drive the FREWLs separately. Hence, intelligent control of the FREWLs improves operational and economic performance based on torque optimization control under different operational conditions.

The longitudinal dynamic model of the FREWLs is shown in Figure 3. This model can be described as follows:

$$m\dot{v}_x = F_{xf} + F_{xr} - R_{xf} - R_{xr} - mg\,\sin\,\alpha - F_x, \tag{1}$$

$$I_e\dot{\omega}_{wf} = T_f - r_{\text{eff}}F_{xf}, \tag{2}$$

$$I_e\dot{\omega}_{wr} = T_r - r_{\text{eff}}F_{xr}, \tag{3}$$

where F_{xf} and F_{xr} are the longitudinal forces of the front and rear tires, R_{xf} and R_{xr} are the rolling resistance forces, m is the mass of the FREWLs, F_x is the longitudinal spading force, T_f and T_r are the driving torques of the front and rear tires, $\dot{\omega}_{wf}$ and $\dot{\omega}_{wr}$ are their angular accelerations, α is the slope, $\dot{v}_x$ is the longitudinal acceleration, I_e is the moment of inertia of the tires, and r_{eff} is their rolling radius.

The rolling resistance forces are as follows:

$$R_{xf} = F_{zf}\cdot f, \tag{4}$$

$$R_{xr} = F_{zr}\cdot f, \tag{5}$$

where f is the rolling resistance coefficient. The vertical forces of the tires are defined as

$$F_{zf} = \frac{m\dot{v}_x h - mgh\,\sin\,\alpha + mgl_r\cos\,\alpha + F_z\left(l_c + l_f + l_r\right)}{l_f + l_r}, \tag{6}$$

$$F_{zr} = \frac{-m\dot{v}_x h + mgh\,\sin\,\alpha + mgl_f\cos\,\alpha - F_z l_c}{l_f + l_r}, \tag{7}$$

where h is the CG height, l_f is the longitudinal distance between the front axle and the CG, l_r is that between the rear axle and the CG, l_c is that between the front axle and the tip of the bucket, and F_z is the vertical spading force.

The vertical forces of the tires are related to their longitudinal forces as [19]

$$F_{xf} = K\sigma_f F_{zf}, \tag{8}$$

$$F_{xr} = K\sigma_r F_{zr}, \tag{9}$$

where K is the tire slip coefficient and σ_f and σ_r are the slip rates of the front and rear tires, respectively. Using $l = l_f + l_r$, $l_l = l_f + l_r + l_c$, and $\lambda = l_r/l$, equations (6) and (7) become

$$F_{zf} = \frac{mh\left(\dot{v}_x - g\,\sin\,\alpha\right)}{l + mg\,\cos\,\alpha\lambda} + \frac{l_l F_z}{l}, \tag{10}$$

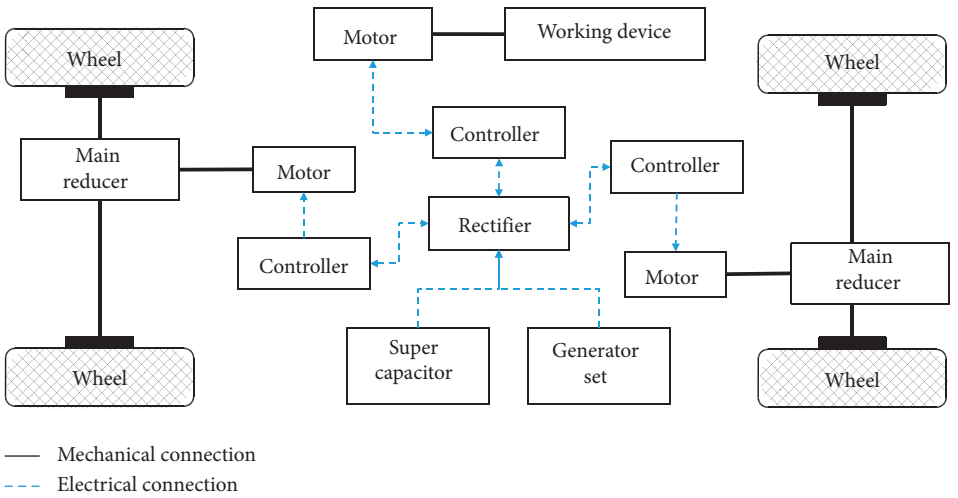

Figure 1: Structure principle of the FREWLs.

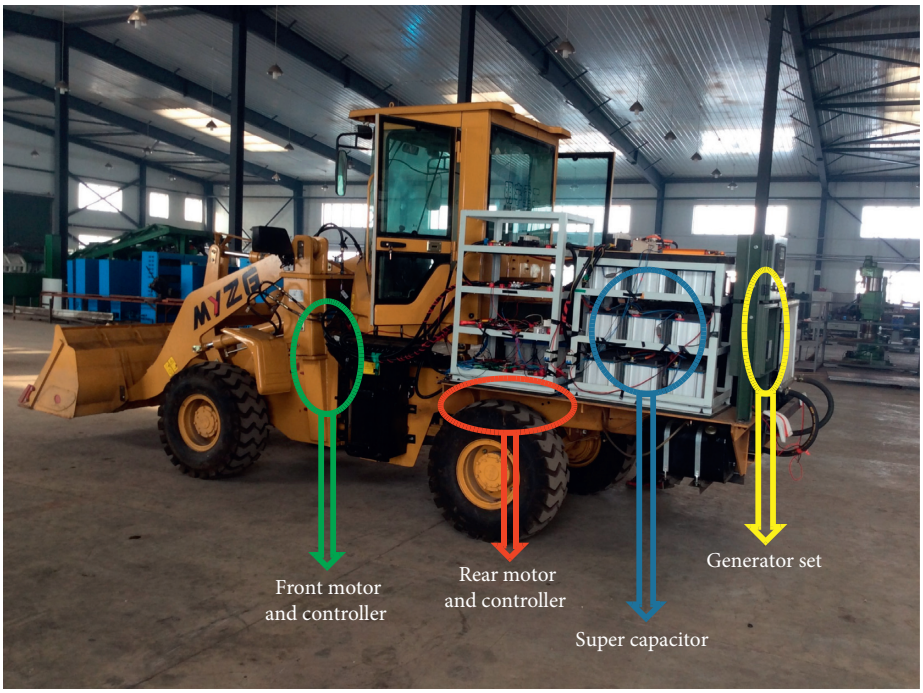

Figure 2: Experimental prototype of FREWLs.

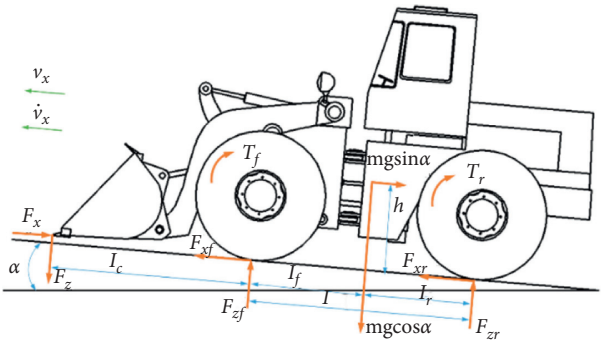

Figure 3: Longitudinal dynamic model of FREWLs.

$$F_{zr} = \frac{-mh(\dot{v}_x - g\ \sin\ \alpha)}{l} + \frac{mg\ \cos\ \alpha(1-\lambda) - l_c F_z}{l}. \quad (11)$$

Equations (1)–(3) can be rewritten based on equations (4)–(11) as

$$\dot{v}_x = \frac{\left(\left(\lambda K\sigma_f + (1-\lambda)K\sigma_r - f\right)g\ \cos\ \alpha - \left(1 + (hK/l)\left(\sigma_f - \sigma_r\right)\right)g\ \sin\ \alpha + \left(F_z/ml\right)\left(K\left(\sigma_f l_l - \sigma_r l_c\right) + f\left(l_c - l_l\right)\right) - \left(F_x/m\right)\right)}{\left(1 - (hK/l)\left(\sigma_f - \sigma_r\right)\right)}, \quad (12)$$

$$\dot{\omega}_{\omega f} = \frac{1}{I_e}\left(T_f - Kr_{eff}\sigma_f\left(\frac{F_z l_l}{l} + g\lambda m\ \cos\ \alpha + \frac{hm}{l}\left(\dot{v}_x - g\ \sin\ \alpha\right)\right)\right), \quad (13)$$

$$\dot{\omega}_{\omega r} = \frac{1}{I_e}\left(T_r + Kr_{eff}\sigma_r\left(\frac{F_z l_c}{l} + g(\lambda - 1)m\ \cos\ \alpha + \frac{hm}{l}\left(\dot{v}_x - g\ \sin\ \alpha\right)\right)\right). \quad (14)$$

In this paper, we assume that all other FREWL parameters are already known or measured. The remaining task is to estimate the CG's longitudinal location and height. The subsequent section uses the superscript "ˆ" to denote estimated parameters.

3. FREWL CG Estimator

3.1. State-Space Model. Equations (12)–(14) can be rewritten as the following estimator with state variable $x_k = \begin{bmatrix} v_x & \omega_f & \omega_r & \widehat{K} & \widehat{h} & \widehat{\lambda} \end{bmatrix}^T$ and the output (measurement) variable $y_k = \begin{bmatrix} v_x & \omega_f & \omega_r \end{bmatrix}^T$:

$$\begin{aligned} x_{k+1} &= F_k(\widehat{p})x_k + L_k(\widehat{p})w_k, \\ y_k &= H_k x_k + v_k, \end{aligned} \quad (15)$$

where $\widehat{p}$ is the vector of unknown parameters, $F_k(\widehat{p})$ is the state-transition matrix, $L_k(\widehat{p})$ is the measurement matrix, w_k and v_k are the process noise, and H_k is the observation matrix. To estimate $\widehat{p}$, it is necessary to expand the state variables to obtain the augmented state vector x_k' [20]:

$$x_k' = \begin{bmatrix} x_k \\ \widehat{p}_k \end{bmatrix}. \quad (16)$$

The estimator of $\widehat{p}_k$ can be changed by the subsequent ISR-UKF when $\widehat{p}_{k+1} = \widehat{p}_k + w_{\widehat{p}_k}$. $w_{\widehat{p}k}$ is a manmade noise with a small value. Hence, equation (12) can be rewritten as

$$\begin{aligned} x_{k+1} &= \begin{bmatrix} F_k(\widehat{p})x_k + L_k(\widehat{p})w_k \\ \widehat{p}_k + w_{\widehat{p}k} \end{bmatrix} = f\left(x_k', w_k, w_{\widehat{p}k}\right), \\ y_k &= \begin{bmatrix} H_k & 0 \end{bmatrix}\begin{bmatrix} x_k \\ \widehat{p}_k \end{bmatrix} + v_k. \end{aligned} \quad (17)$$

The relationship between the state variables x_{k+1} and x_k can be expressed as [21]

$$x_{k+1} = x_k + \Delta t \cdot \dot{x}_k, \quad (18)$$

where Δt is the sampling time. Equation (18) is actually a first-order approximation of the real system. According to equations (12), (13), (17), and (18), the state-space model for ISR-UKF can be defined as

$$\begin{aligned} \begin{bmatrix} v_{x,k+1} \\ \omega_{f,k+1} \\ \omega_{r,k+1} \\ \widehat{K}_{k+1} \\ \widehat{h}_{k+1} \\ \widehat{\lambda}_{k+1} \end{bmatrix} &= \begin{bmatrix} v_{x,k} + \Delta t \cdot \dot{v}_{x,k} \\ \omega_{f,k} + \Delta t \cdot \dot{\omega}_{f,k} \\ \omega_{r,k} + \Delta t \cdot \dot{\omega}_{r,k} \\ \widehat{K}_k \\ \widehat{h}_k \\ \widehat{\lambda}_k \end{bmatrix} + \begin{bmatrix} w_{k+1}^{v_x} \\ w_{k+1}^{\omega_f} \\ w_{k+1}^{\omega_r} \\ w_{k+1}^{K} \\ w_{k+1}^{h} \\ w_{k+1}^{\lambda} \end{bmatrix}, \\ y_k &= \begin{bmatrix} 1 & 0 & 0 & 0 & 0 & 0 \\ 0 & 1 & 0 & 0 & 0 & 0 \\ 0 & 0 & 1 & 0 & 0 & 0 \end{bmatrix}\begin{bmatrix} v_{x,k} \\ \omega_{f,k} \\ \omega_{r,k} \\ \widehat{K}_k \\ \widehat{h}_k \\ \widehat{\lambda}_k \end{bmatrix} + \begin{bmatrix} e_k^{v_x} \\ e_k^{\omega_f} \\ e_k^{\omega_r} \end{bmatrix}, \end{aligned} \quad (19)$$

where w_k^i and e_k^i are the white noise.

3.2. ISR-UKF Algorithm. ISR-UKF algorithm requires initial $\widehat{x}$ and P_0 values to be given to the state variable and covariance, respectively:

$$\begin{aligned} \widehat{x}_0 &= E[x_0], \\ P_0 &= \mathrm{chol}\left\{E\left[\left(x_0 - \widehat{x}_0\right)\left(x_0 - \widehat{x}_0\right)^T\right]\right\}. \end{aligned} \quad (20)$$

Calculate Sigma point which includes $2n + 1$ points:

$$x_{k|k} = \begin{cases} x^{(0)} = \widehat{x}, & i = 0, \\ x^{(i)} = \widehat{x} + \left(\sqrt{(n+\lambda)P_k}\right), & i = 1 \sim n, \\ x^{(i)} = \widehat{x} - \left(\sqrt{(n+\lambda)P_k}\right), & i = n+1 \sim 2n. \end{cases} \quad (21)$$

The weight of the Sigma point is

$$\omega_m^{(0)} = \frac{\lambda}{(n+\lambda)},$$
$$\omega_c^{(0)} = \frac{\lambda}{(n+\lambda)+\left(1-\alpha^2+\beta\right)}, \quad (22)$$
$$\omega_m^{(i)} = \omega_c^{(i)} = \frac{\lambda}{2(n+\lambda)}, \quad i = 1 \sim 1n,$$

where ω_c is the weight of covariance, ω_m is the weight of the mean value, λ is the a parameter defining $\lambda = \alpha^2(n+\kappa) - n$, α is a constant, κ is the parameter which ensures that $(n+\lambda)P_k$ is a positive semidefinite matrix, and β is a nonnegative weight.

The further predictions of the state variable and covariance are as follows:

$$\widehat{x}_{k+1|k} = \sum_{i=0}^{2n} \omega_i^{(m)} x_{k+1|k}^{(i)},$$
$$P_{k+1|k} = qr\left\{\left[\sqrt{\omega_1^{(c)}}\left(x_{k+1|k}^1 - x_{k+1|k}^0\right)\right]\sqrt{\omega_{2n}^{(c)}}\left(x_{k+1|k}^{2n} - x_{k+1|k}^0\sqrt{Q}\right)^T\right\}, \quad (23)$$

where Q_k is the process noise. The predicted measurement value of Sigma is

$$y_{k+1|k}^{(i)} = Hx_{k+1|k}^{(i)}. \quad (24)$$

Based on equations (22) and (24), the mean measurement value is

$$\widehat{y}_{k+1|k} = \sum_{i=0}^{2n} \omega_i^{(m)} y_{k+1|k}^{(i)}. \quad (25)$$

In order to maintain the update of state variable estimation, the covariance of further prediction is

$$P_{yk} = qr\left\{\left[\sqrt{\omega_1^c}\left(y_{k+1|k}^1 - y_{k+1|k}^0\right)\sqrt{\omega_{2n}^c}\left(y_{k+1|k}^{2n} - y_{k+1|k}^0\right)\sqrt{R}\right]^T\right\},$$
$$P_{xk,yk} = \sum_{i=0}^{2n} \omega_i^{(c)}\left[x_{k+1|k}^{(i)} - \widehat{x}_{k+1|k}\right]\left[y_{k+1|k}^{(i)} - \widehat{y}_{k+1|k}\right].^T \quad (26)$$

Calculate the gain matrix K_k:

$$K_k = \left(\frac{P_{xk,yk}}{P_{yk}^T}\right)P_{yk}. \quad (27)$$

The subsequent updates of the state variable and covariance are as follows:

$$\widehat{x}_{k+1|k+1} = \widehat{x}_{k+1|k} + K_k\left(y_{k+1|k+1} - \widehat{y}_{k+1|k}\right),$$
$$F_k = \left(P_{k+1|k}\right)^T H_k^T,$$
$$U_k = \left[F_k^T F_k + R_k\right]^{1/2}, \quad (28)$$
$$P_{k+1|k+1} = P_{k+1|k}\left[I - F_k\left(U_k^T\right)^{-1}\left(U_k + \sqrt{R_k}\right)^{-1}F_k^T\right].$$

The above calculation procedures constitute a completed ISR-UKF algorithm.

4. Simulation Results and Analysis

The typical working condition of FREWLs is different from that of other vehicles, and it is more driving on the bumpy road. Hence, two simulation conditions are designed to verify our estimation method. Condition 1 is driving on a bumpy road. Condition 2 is spading on a bumpy road. An extra continuous force on the tip of the bucket simulates the longitudinal spading force from 5 to 7 s. The simulation parameters are shown in Table 1.

4.1. Driving Conditions on a Bumpy Road. The longitudinal speed, CG longitudinal location, and CG height simulation results are shown, respectively, in Figures 4(a)–4(c) when the FREWL is driving on a bumpy road. Because the FREWL drives continuously on this road, numerical fluctuations of the longitudinal speed and CG longitudinal location are more frequently compared to flat road in Figures 4(a) and 4(b). The CG longitudinal location fluctuates greatly and is more susceptible to the influence of acceleration and deceleration. In the green circle, the CG longitudinal location moves backward when the FREWL accelerates. Due to FREWL's deceleration, the CG longitudinal location moves forward in the brown circle. In addition, the change in the CG height is less with relatively drastic change compared to CG longitudinal location in speed in Figure 4(c). The maximum errors in the CG longitudinal location and CG height between the estimated and reference values are 10.2% and 4.2%, respectively.

4.2. Spading Conditions on a Bumpy Road. Figures 5(a)–5(c) show the longitudinal speed, CG longitudinal location, and CG height simulation results when the FREWL is spading on a bumpy road. The CG location estimation effect remains acceptable. The CG longitudinal location changes with the road gradient before 5 s in Figures 5(a) and 5(b). Due to the fact that longitudinal spading force hinders driving, the longitudinal speed declines from 5 s to 8 s and the CG's longitudinal location moves forward in a brown circle. With the FREWL accelerating, the CG's longitudinal location changes in a wavelike manner on the bumpy road from 8.2 to 10 s. The CG height still changes slightly, as influenced by the changing of the longitudinal speed in Figure 5(c).

5. Experimental Results and Analysis

Because FREWL is a novel hybrid loader, the static position of the CG must be remeasured by a professional electronic scale as an experimental reference. The processes of the static measurement and real-time estimation methods are shown in Figure 6.

FREWL has undergone a major hardware restructuring, and some components are no longer reliable. The generator set and supercapacitor of the FREWLs have high voltages and are designed to work above 280 V. To ensure the safety of drivers and FREWLs, the driving longitudinal speed is slow on asphalt roads, and no spading experiments were

Table 1: Set values of simulation parameters.

Simulation parameters	Set value	Units
m	4.7	kg
K	19	—
r_{eff}	0.55	m
I_e	3.33	—
Δt	0.01	—
T_{mf}	50	N·m
T_{mr}	50	N·m
F_x	600	N
α	0.01	—
β	2	—
κ	0	—

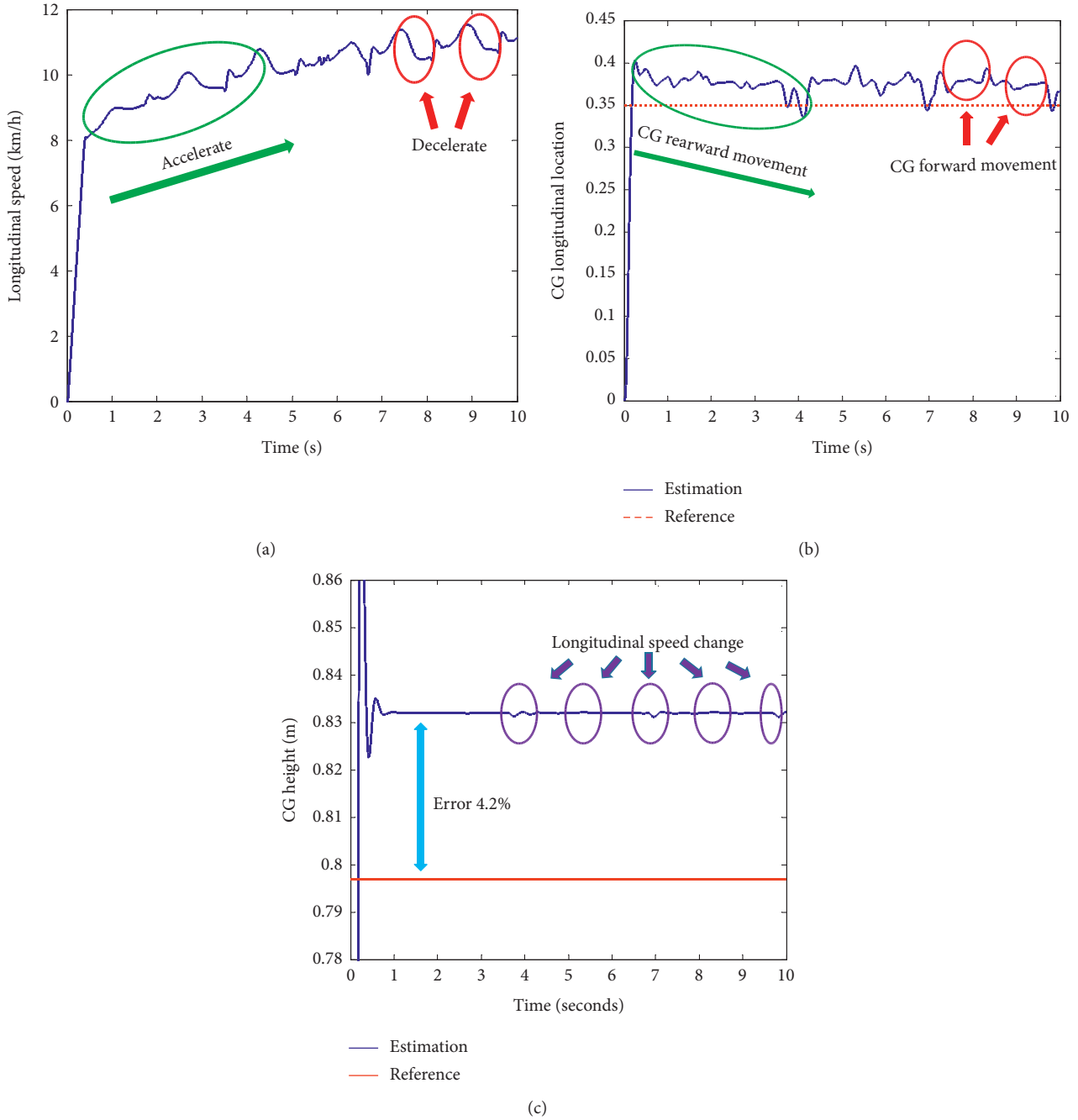

Figure 4: Simulation results for driving conditions on a bumpy road. (a) Longitudinal speed. (b) CG longitudinal location. (c) CG height.

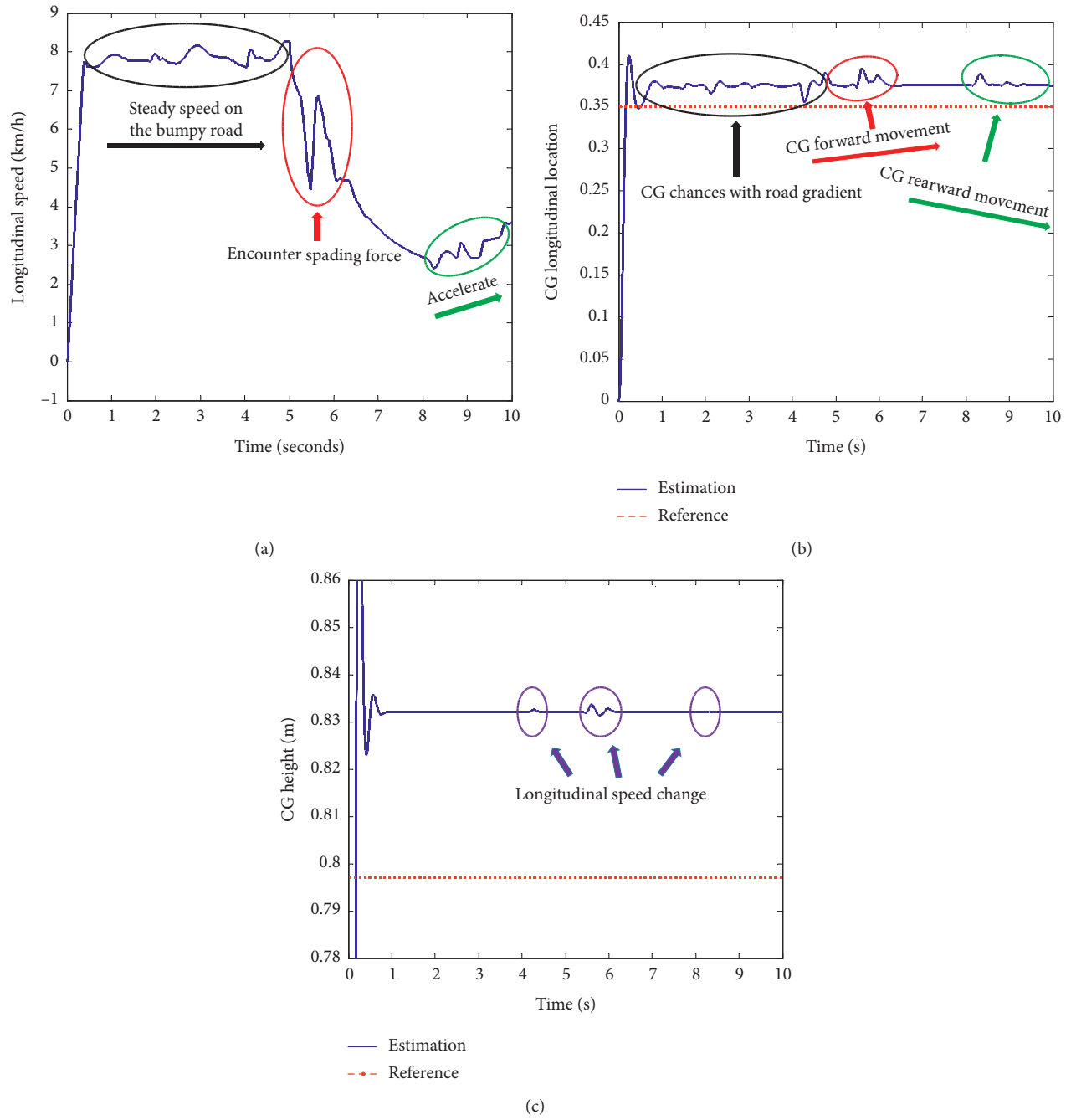

FIGURE 5: Simulation results during driving with spading conditions on a bumpy road. (a) Longitudinal speed. (b) CG longitudinal location. (c) CG height.

conducted. The front and rear motors output the same power. Two experimental conditions are designed to verify the CG estimation method: (a) constant-torque experimentation and (b) acceleration and deceleration experiments.

5.1. Constant-Torque Experiment. The front motor power output and the longitudinal speed are shown in Figures 7(a) and 7(b), respectively. The experiment is designed to observe the performance of the CG estimation method for a FREWL undergoing uniform acceleration. The output torque of the front motor is approximately maintained at 32 N·m from 4 s to 14 s. The value of the CG longitudinal location begins to decrease when the FREWL accelerates, as shown in Figures 7(b) and 7(c). Once the FREWL starts to decelerate, the CG longitudinal location increases immediately. The maximum error between the estimated and reference values for this location is 6.0% in the data stabilization phase in Figure 7(c). The maximum error in the CG height between the estimated and reference values is 4.6% in the data stabilization phase in Figure 7(d). In this working condition,

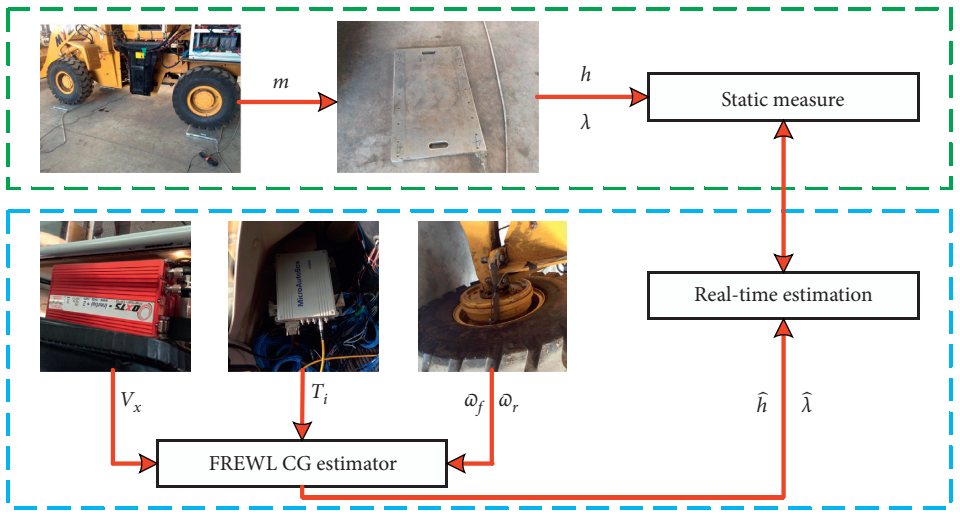

Figure 6: Two measurement methods used in the experiment.

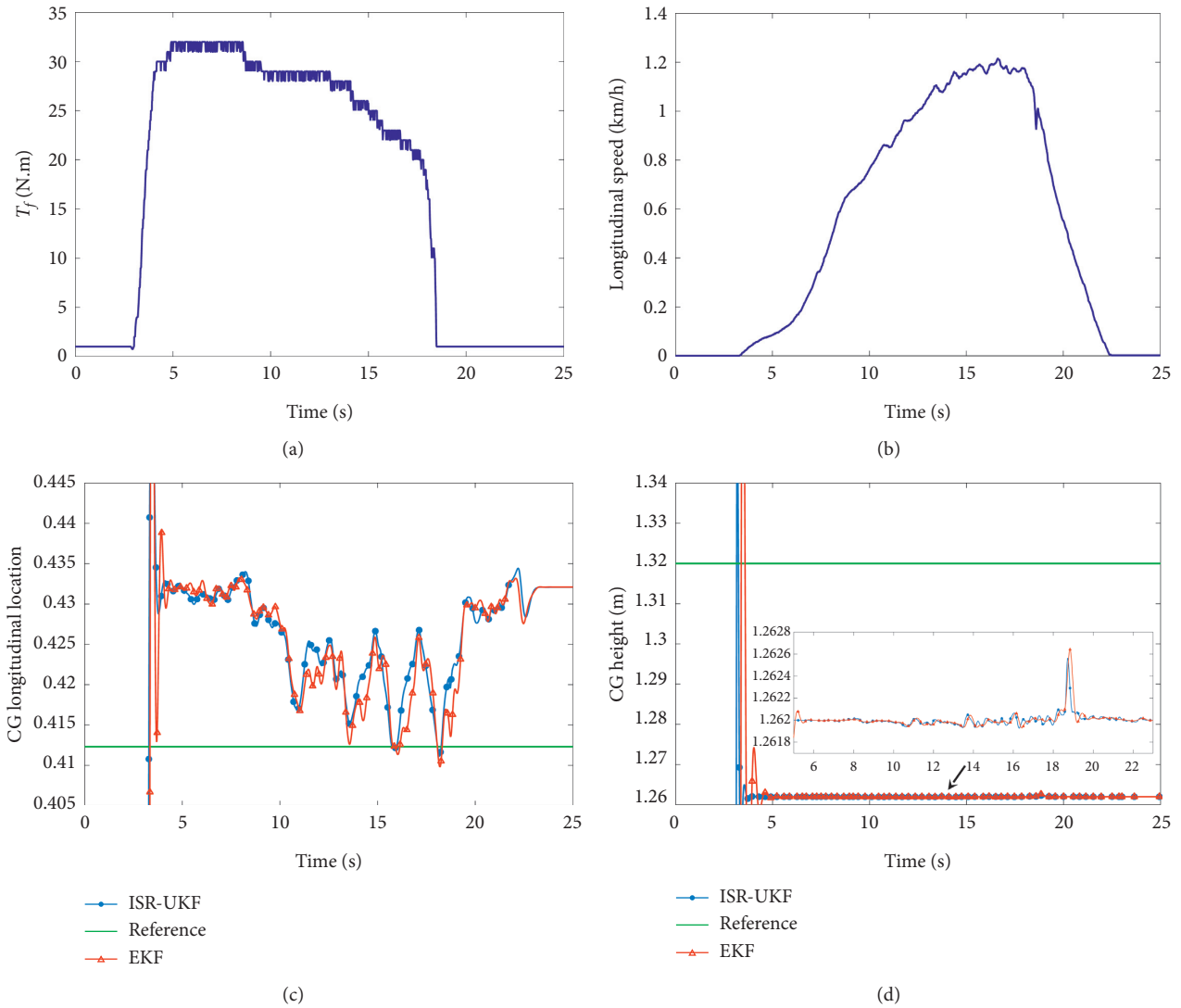

Figure 7: Constant-torque experiment. (a) Output torque of the front motor; (b) longitudinal speed; (c) CG longitudinal location; (d) CG height.

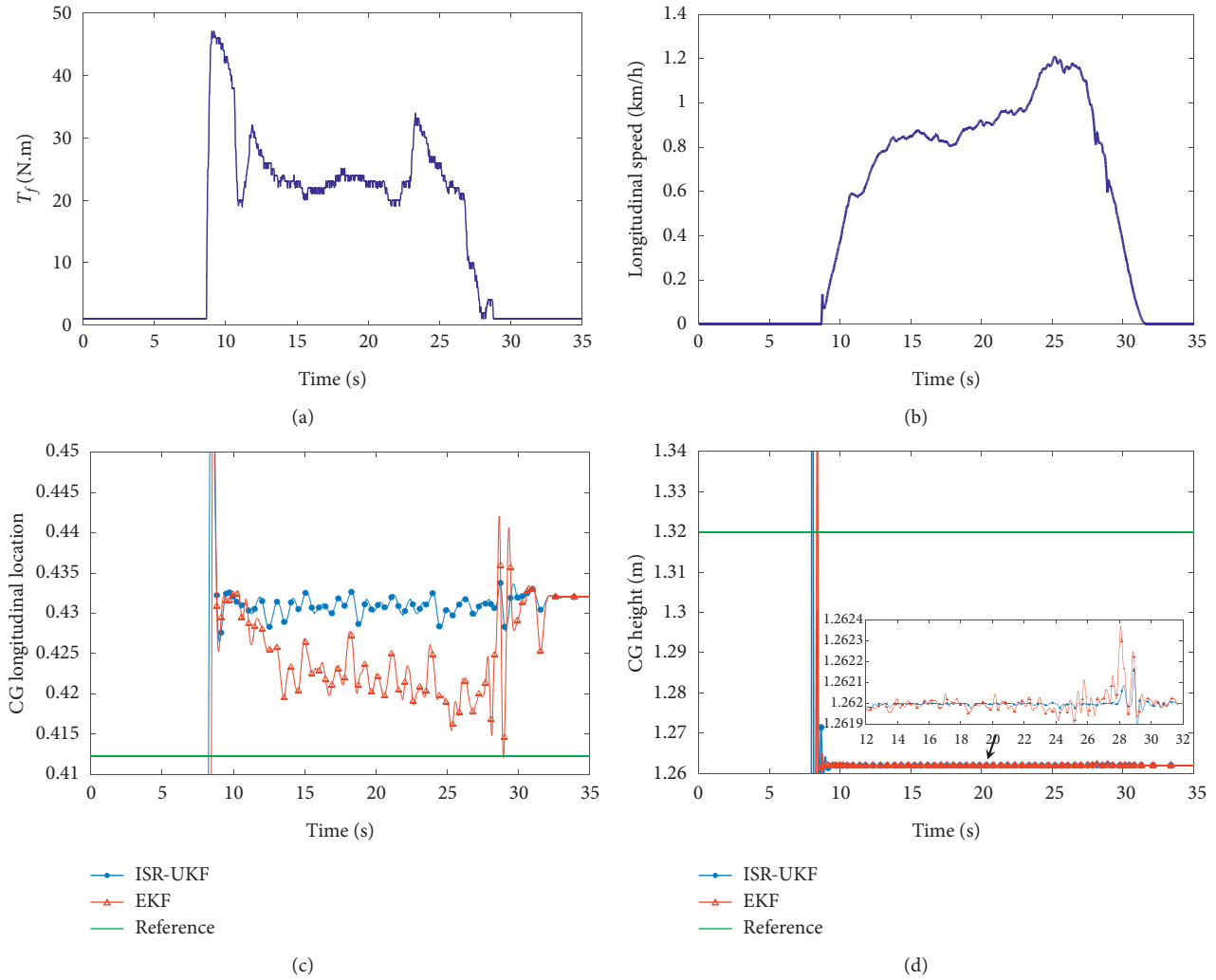

FIGURE 8: Acceleration and deceleration experiment. (a) Output torque of the front motor; (b) longitudinal speed; (c) CG longitudinal location; (d) CG height.

both ISR-UKF and EKF can realize dynamic estimation with high accuracy due to the small variation of velocity, motor output torque, and other values. Relatively speaking, the numerical vibration of EKF is more intense due to its own algorithm.

5.2. Acceleration and Deceleration Experiments. The fluctuation of the CG height is quite small and that in the longitudinal location is relatively large in the constant-torque experiment. To further determine the effectiveness of CG longitudinal location estimation and acceleration and deceleration experiments, more complex driving conditions are designed. The power output of the front motor and longitudinal velocity are shown in Figures 8(a) and 8(b), respectively. The value of the CG longitudinal location and height changes with the longitudinal speed in Figures 8(c) and 8(d). Compared with the constant-torque experiment, ISR-UKF has higher estimation accuracy and stability than EKF due to frequent changes in motor output torque. Due to the limitations of the EKF algorithm, the estimated value tends to diverge over time.

The velocity has the largest change from 24 s to 28 s. Hence, the value of the CG longitudinal location experiences maximal fluctuation compared to other times. This situation is consistent with the change of the actual CG. The CG height still changes with the braking in Figure 8(d).

6. Discussion

This paper proposes a novel real-time CG estimation method for FREWLs. This method is suitable for FREWLs operating under driving and spading conditions on bumpy roads. The simulation and experimental results demonstrate the validity of this method. However, errors exist between the estimated and reference values. There are several possible reasons for these errors:

(i) The static reference is calculated as the average of 10 measurements. Hence, the static reference may have

a computational error because of the lack of more professional testing equipment.

(ii) The initial value of ISR-UKF may affect the estimation.

(iii) The value of the noise-covariance matrix influences estimated effect and estimated accuracy. The numerical selection of the noise-covariance matrix is also a hot research area [22–24].

(iv) Because of the lack of ABS systems in FREWLs, a hall sensor was used to measure wheel speed. Hence, the measurement accuracy may be lower. Dramatic changes in the input parameters of the estimation model affect the changes in the value of the output parameters, resulting in poor stability.

(v) FREWLs usually drive at low speed, so air resistance with a very small value is usually ignored in the dynamical model. However, air resistance also affects estimation performance.

All of the above may lead to errors. However, the errors fall within acceptable limits.

In addition, this approach has many challenges in practice:

(i) The spading force cannot presently be known in real time. The traditional spading force calculation is based on empirical formulas. From the cylinder pressure and force analysis of a working device, the spading force is likely to be calculated in real time in the future.

(ii) The FREWL's CG is also affected by lateral motion. However, the main consideration is longitudinal motion in this paper.

(iii) To ensure the safety of drivers and FREWLs, the spading condition was not tested experimentally.

(iv) The estimated value basically converges to the reference value in the experiment. However, it remains to be proven whether the fluctuating value is reasonable. Current equipment has difficulties in verifying the exact location of the CG in real time. The subsequent intelligent control of the FREWLs is possibly to be verified in the future.

(v) The structure, operating environment, and operating characteristics of the wheel loader determine that, compared with the vehicle, vehicle parameters such as speed, acceleration, position of CG, and longitudinal force of tires change in a faster frequency and a larger range. The robustness of the algorithm seems insufficient from the simulation and experiment results. There are probably main reasons:

(1) In the simulation, the estimated value fluctuates greatly because the road is set on uneven road and the vehicle driving is bumpy. At the same time, the simulation also simulates the spading resistance during operation, which has a great influence on the numerical variation of simulation parameters.

(2) In the experiment, because the FREWL is a modified loader and the suspension system has poor shock absorption performance, the FREWL also bumps violently in the process of driving, which significantly affects the variation of the estimated value.

In the later research, we will try to add global sliding mode theory [25] or adaptive second-order sliding mode [26] on the basis of the existing algorithm, so as to better increase the estimated stability.

7. Conclusion

Our novel real-time CG estimation method for FREWLs exhibits accurate performance under simulation and experimental conditions. The simulation conditions include driving and spading on bumpy roads. Experimental conditions comprise a constant-torque experiment and an acceleration-and-deceleration experiment.

The important feature of the proposed real-time estimation method is that it is suitable for FREWL dynamics and operational characteristics and that it enhances our ability to solve strong nonlinear problems while avoiding the problem of a negative-definite Cholesky factor. The estimated value of the CG basically converges to the reference value in the simulation and experiment. These results indicate that fluctuation of the CG height is smaller compared with the CG longitudinal location. Once the FREWL accelerates, the CG moves backward and the value of the CG's longitudinal location immediately decreases. With different accelerations and decelerations, the CG longitudinal location differs.

The evaluated errors between the estimated and reference values in the experiment may have several sources, including static reference error, the effects of the initial value and the noise-covariance matrix, the sensor error, and simplification of the dynamical model. Moreover, there are still many challenges facing the practical application of this method. These sources of error and challenges will be researched in the future. In particular, the spading force needs to be accurately calculated or estimated in real time under operating conditions.

Data Availability

The data used to support the findings of this study are included within the article.

Conflicts of Interest

The authors declare that there are no conflicts of interest regarding the publication of this paper.

Acknowledgments

This work was supported by the Science and Technology Research Program of Chongqing Municipal Education Commission (Grant no. KJQN201800812), the Open Project of Research Platform of Chongqing Technology and

Business University (Grant no. KFJJ2018056), and the Research Project of Chongqing Technology and Business University (Grant no. 1952020), China.

References

[1] J. X. Wang, Z. Y. Yang, S. K. Liu, Q. Zhang, and Y. Han, "A comprehensive overview of hybrid construction machinery," *Advances in Mechanical Engineering*, vol. 8, no. 3, 2016.

[2] J. Gu and D. Seward, "Improved control of intelligent excavator using proportional-integral-plus gain scheduling," *Journal of Central South University of Technology*, vol. 19, no. 2, pp. 384–392, 2012.

[3] S. K. Kim, "A path generation method considering the work behavior of operators for an intelligent excavator," *Journal of the Korean Society of Civil Engineers D*, vol. 30, no. 4, pp. 433–442, 2010.

[4] X. Ding, Z. Wang, L. Zhang, and C. Wang, "Longitudinal vehicle speed estimation for four-wheel-independently-actuated electric vehicles based on multi-sensor fusion," *IEEE Transactions on Vehicular Technology*, vol. 69, no. 11, pp. 12797–12806, 2020.

[5] C. Wang, Z. Wang, L. Zhang, D. Cao, and D. G. Dorrell, "A vehicle rollover evaluation system based on enabling state and parameter estimation," *IEEE Transactions on Industrial Informatics*, vol. 17, no. 6, pp. 4003–4013, 2020.

[6] Q. Wang, Y. Zhao, Y. Deng, H. Xu, H. Deng, and F. Lin, "Optimal coordinated control of ARS and DYC for four-wheel steer and in-wheel motor driven electric vehicle with unknown tire model," *IEEE Transactions on Vehicular Technology*, vol. 69, no. 10, pp. 10809–10819, 2020.

[7] J. Lee, D. Hyun, K. Han, and S. Choi, "Real-time longitudinal location estimation of vehicle center of gravity," *International Journal of Automotive Technology*, vol. 19, no. 4, pp. 651–658, 2017.

[8] S. S. Kim, "A experimental study on the measurement and estimation of vehicle center of gravity," *The Korean Society of Automotive Engineers*, vol. 18, no. 5, pp. 91–99, 2010.

[9] X. Y. Huang and J. M. Wang, "EKF-based vehicle center of gravity position real-time estimation in longitudinal maneuvers with road course elevation," in *Proceedings of the 5th Annual Dynamic Systems and Control Division Conference/11th JSME Motion and Vibration Conference*, pp. 665–672, Palo Alto, CA, USA, October 2013.

[10] X. Huang and J. Wang, "Center of gravity height real-time estimation for lightweight vehicles using tire instant effective radius," *Control Engineering Practice*, vol. 21, no. 4, pp. 370–380, 2013.

[11] X. Huang and J. Wang, "Real-time estimation of center of gravity position for lightweight vehicles using combined AKF-EKF method," *IEEE Transactions on Vehicular Technology*, vol. 63, no. 9, pp. 4221–4231, 2014.

[12] H. Yue, L. Zhang, H. Shan, H. Liu, and Y. Liu, "Estimation of the vehicle's centre of gravity based on a braking model," *Vehicle System Dynamics*, vol. 53, no. 10, pp. 1520–1533, 2015.

[13] M. S. Chen, G. D. Yin, N. Zhang, and J. Chen, "Joint estimation of center of gravity position and mass for the front and rear independently driven electric vehicle with payload in the start stage," in *Proceedings of the 35th Chinese Control Conference*, pp. 932–1937, IEEE, Chengdu, China, July 2016.

[14] Z. T. Yu and J. M. Wang, "Simultaneous estimation of vehicle's center of gravity and inertial parameters based on Ackermann's steering geometry," *Journal of Dynamic Systems Measurement and Control-Transactions of the ASME*, vol. 139, no. 3, 2017.

[15] C. Lin, X. Gong, R. Xiong, and X. Cheng, "A novel H ∞ and EKF joint estimation method for determining the center of gravity position of electric vehicles," *Applied Energy*, vol. 194, pp. 609–616, 2017.

[16] J. Liu and X. S. Gu, "State estimation of a solid-state polymerization reactor for PET based on improved SR-UKF," *ASIA-Pacific Journal of Chemical Engineering*, vol. 5, no. 2, pp. 378–389, 2010.

[17] S. Vellayikot and M. V. Vaidyan, "Experimental investigations on performance comparison of EKF and ANN based controllers with UKF based controller for autonomous hybrid systems with uncertainties," *Journal of Electrical Engineering and Technology*, vol. 11, no. 5, pp. 1492–1502, 2016.

[18] L. D'Alfonso, W. Lucia, P. Muraca, and P. Pugliese, "Mobile robot localization via EKF and UKF: a comparison based on real data," *Robotics and Autonomous Systems*, vol. 74, pp. 122–127, 2015.

[19] X. Y. Huang and J. M. Wang, "Payload parameter real-time estimation for lightweight vehicles," in *Proceedings of the ASME Dynamic Systems and Control Conference/Bath/ASME Symposium on Fluid Power and Motion Control*, pp. 733–740, Fort Lauderdale, FL, USA, May 2012.

[20] D. Simon, *Optimal State Estimation: Kalman, H Infinity, and Nonlinear Approaches*, John Wiley & Sons, Hoboken, NJ, USA, 2006.

[21] K. Charles and G. R. Chen, *Kalman Filtering: With Real-Time Applications*, Springer Science & Business Media, New York, NY, USA, 2013.

[22] A. Rahimi, K. D. Kumar, and H. Alighanbari, "Fault estimation of satellite reaction wheels using covariance based adaptive unscented Kalman filter," *ACTA Astronautica*, vol. 134, pp. 159–169, 2017.

[23] A. Nakabayashi and G. Ueno, "An extension of the ensemble Kalman filter for estimating the observation error covariance matrix based on the variational bayes's method," *Monthly Weather Review*, vol. 145, no. 1, pp. 199–213, 2017.

[24] I. Hashlamon and K. Erbatur, "An improved real-time adaptive Kalman filter with recursive noise covariance updating rules," *Turkish Journal of Electrical Engineering & Computer Sciences*, vol. 24, no. 2, pp. 524–540, 2016.

[25] L. Zhang, Y. Wang, and Z. Wang, "Robust lateral motion control for in-wheel-motor-drive electric vehicles with network induced delays," *IEEE Transactions on Vehicular Technology*, vol. 68, no. 11, pp. 10585–10593, 2019.

[26] L. Zhang, H. Ding, J. Shi et al., "An adaptive backstepping sliding mode controller to improve vehicle maneuverability and stability via torque vectoring control," *IEEE Transactions on Vehicular Technology*, vol. 69, no. 3, pp. 2598–2612, 2020.